

Gravitational waves from eccentric binary neutron star mergers: Systematic biases induced by quasi-circular templates

Giulia Huez¹, Sebastiano Bernuzzi¹, Matteo Breschi¹, and Rossella Gamba^{2,3}

¹*Theoretisch-Physikalisches Institut, Friedrich-Schiller-Universität Jena, 07743, Jena, Germany*

²*Institute for Gravitation & the Cosmos, The Pennsylvania State University, University Park PA 16802, USA*

³*Department of Physics, University of California, Berkeley, CA 94720, USA*

(Dated: April 29, 2025)

The use of quasi-circular waveforms in matched-filter analyses of signals from eccentric binary neutron star (BNS) mergers can lead to biases in the source’s parameter estimation. We demonstrate that significant biases can be present already for moderate eccentricities $e_0 \gtrsim 0.05$ and LIGO-Virgo-Kagra signals with signal-to-noise ratio (SNR) $\gtrsim 12$. We perform systematic Bayesian mock analyses of unequal-mass non-spinning BNS signals up to eccentricities $e_0 \sim 0.1$ using quasi-circular effective-one-body (EOB) waveforms with spins. We find fractional SNR losses up to tens of percent and up to $16\text{-}\sigma$ deviations in the inference of the chirp mass. The latter effect is sufficiently large to lead to an incorrect (and ambiguous) source identification. The inclusion of spin precession in the quasi-circular waveform does not capture eccentricity effects. We conclude that high-precision observations with advanced (and next generation) detectors are likely to require standardized, accurate, and fast eccentric waveforms.

I. INTRODUCTION

The observed BNS in the Milky Way have a wide range of eccentricities [1, 2]. A short-period, highly eccentric sub-population that includes the Hulse-Taylor binary has eccentricity up to ~ 0.8 . By the time of merger, field binaries are expected to circularize and to enter the sensitivity band of ground-based Gravitational wave (GW) detectors at about 10 Hz with negligible eccentricity $e_0 \lesssim 10^{-4}$. However, in case a highly eccentric sub-population is formed in more dynamical environment, the binaries might retain a non-negligible eccentricity at merger. BNS searches with quasi-circular templates are expected to be effectual up to $e_0 \lesssim 0.05$ [3]. A recent search for eccentric signals placed a 90% upper limit of ~ 1700 mergers $\text{Gpc}^{-3}\text{Yr}^{-1}$ for eccentricities BNS $\lesssim 0.43$ at 10 Hz [4, 5] (Cf. *e.g.* [6, 7] for eccentric binary black hole (BBH) searches).

The BNS signals GW170817 and GW190425 detected by the LIGO-Virgo collaboration [8–10] have been found and analyzed with quasi-circular GW templates. Their eccentricities are (or are assumed) sufficiently small so that inference with quasi-circular templates does not affect the source parameters. An eccentric parameter estimation of the two signals using a post-Newtonian (PN) Taylor F2 approximant indicates upper limits of $e_0 \leq 0.024$ and $e_0 \leq 0.048$ for GW170817 and GW190925 respectively at 90% confidence level [11]. The direct parameter estimation (PE) with eccentric templates increases the upper limit of a factor three when compared to estimates with more approximated methods [12].

Several recent studies have analyzed eccentricity in BBH observations [12–20]. Some of them suggest that signals from highly eccentric mergers and/or head-on collisions may be confused with mildly precessing quasi-circular binaries [17, 21, 22]. This degeneracy might be particularly relevant for events like GW190521 but could in principle play a role also in the interpretation of bi-

naries with lower masses, including BNS. However, the systematics in GW PE for the latter signals are not yet fully understood.

Favata et al. [23] assessed the detectability and biases in BNS eccentricity measurement using spin-aligned PN models and Fisher matrix. They find that a measurement of eccentricity better than 30% (1-sigma fractional error) requires eccentricity values larger than 0.01 at 10 Hz. Low frequency sensitivity is particularly relevant for eccentricity measurements. Systematic errors become comparable to these statistical errors for eccentricities as low as 0.01. One of the main reasons for this bias is a (Newtonian) degeneracy with the chirp mass. Cho [24] performed Bayesian PEs of non-spinning eccentric signal with $e_0 \leq 0.025$ using non-spinning TaylorF2 quasi-circular waveforms. They find the use of circular templates introduce systematic biases in the intrinsic parameters (chirp mass, symmetric mass ratio and tidal parameters) and calculate the distributions of the biases with Markov-Chain-Monte-Carlo methods (for the considered range of eccentricities).

Compact binaries analyses of eccentric signals rely on the availability of accurate waveform models. Several binary black holes models are available [25–34] and have been adopted in searches and parameter estimation, *e.g.* [13, 17, 19, 20, 22, 35–38]. Among them, the EOB **TEOBResumS-Dalí** can generate waveforms for generic compact binaries and arbitrary orbits [39, 40]. **TEOBResumS-Dalí** incorporates tidal effects and can thus generate BNS waveforms for eccentric and spin-precessing mergers.

In this work, we consider non-spinning unequal-mass BNS signals up to eccentricities $e_0 \sim 0.1$ and perform full Bayesian mock analyses using quasi-circular templates with either non-precessing or precessing spin effects. Focusing on a case study that has intrinsic parameters compatible with GW170817 (including the eccentricity), we demonstrate the biases in the inference of source param-

ters caused by neglecting non-circular effects in the waveform model.

The paper is structured as follows. In Sec. II, we introduce the framework employed for the simulation of the signals and the relative analyses. We present the results we obtained, with a comparison between non-precessing and spin-precessing effects in Sec. III. Finally in Sec. IV we summarize and conclude.

Conventions – We use geometric units $c = G = 1$ with masses expressed in solar masses M_\odot or explicitly state units. The binary mass is $M = m_1 + m_2$, where $m_{1,2}$ are the masses of the two stars, the mass ratio $q = m_1/m_2 \geq 1$, and the symmetric mass ratio $\nu = m_1 m_2 / M^2$. The chirp mass is $\mathcal{M} = \nu^{3/5} M$. The dimensionless spin vectors are denoted with $\vec{\chi}_i$ for $i = 1, 2$ and the orbital angular momentum with \vec{L} .

The spin parameters parallel and perpendicular to $\hat{n} = \vec{L}/||\vec{L}||$ are

$$\chi_{\text{eff}} := \frac{m_1}{M} \vec{\chi}_1 \cdot \hat{n} + (1 \leftrightarrow 2) \quad (1)$$

and

$$\chi_p := \max \left(\chi_{1,\perp}, \frac{1}{q} \frac{4+3q}{4q+3} \chi_{2,\perp} \right) \quad (2)$$

where $\chi_{i,\perp} = |\vec{\chi}_i - (\vec{\chi}_i \cdot \hat{n}) \hat{n}|$ for $i = 1, 2$. The quadrupolar tidal polarizabilities are defined as $\Lambda_i = (2/3) k_{2,i} C_i^{-5}$ for $i = 1, 2$, where $k_{2,i}$ and C_i are respectively the $\ell = 2$ gravitoelectric Love number and the compactness of the i -th neutron star (NS). The reduced tidal parameter [41],

$$\tilde{\Lambda} := \frac{16}{13} \left[\frac{(m_1 + 12m_2)m_1^4 \Lambda_1}{M^5} + (1 \leftrightarrow 2) \right], \quad (3)$$

determines the strength of the leading-order tidal contribution to the binary interaction potential, while the parameter

$$\delta \tilde{\Lambda} := \left[1 - \frac{7996}{1319} \frac{m_2}{m_1} - \frac{11005}{1319} \left(\frac{m_2}{m_1} \right)^2 \right] \frac{m_1^6 \Lambda_1}{M^6} - (1 \leftrightarrow 2), \quad (4)$$

determines the next-to-leading order contribution for asymmetric binaries.

The GW polarizations h_+ and h_\times , plus and cross respectively, are decomposed in (ℓ, m) multipoles as

$$h_+ - i h_\times = D_L^{-1} \sum_{\ell=2}^{\infty} \sum_{m=-\ell}^{\ell} h_{\ell m}(t) {}_{-2}Y_{\ell m}(\iota, \varphi), \quad (5)$$

where D_L is the luminosity distance, ${}_{-2}Y_{\ell m}$ are the $s = -2$ spin-weighted spherical harmonics and ι, φ are respectively the polar and azimuthal angles that define the orientation of the binary with respect to the observer. Each mode $h_{\ell m}(t)$ is decomposed in amplitude $A_{\ell m}(t)$ and phase $\phi_{\ell m}(t)$, as

$$h_{\ell m}(t) = A_{\ell m}(t) e^{-i\phi_{\ell m}(t)}, \quad (6)$$

with a related GW frequency, $\omega_{\ell m}(t) = 2\pi f_{\ell m}(t) = \dot{\phi}_{\ell m}(t)$. If the multipolar indices (ℓ, m) are omitted from a multipolar quantity, we implicitly refer to the dominant $(2, 2)$ mode.

The Fourier transform of a time-domain signal $h_{\ell m}(t)$ is indicated as $\tilde{h}_{\ell m}(f)$ and defined as

$$\tilde{h}_{\ell m}(f) = \int_{-\infty}^{+\infty} h_{\ell m}(t) e^{-2\pi i f t} dt. \quad (7)$$

Analogously to the time-domain case, the frequency series $\tilde{h}_{\ell m}(f)$ can be decomposed in amplitude and phase. The numbers quoted from the posterior probabilities refer to the median of the distributions and the 90% confidence intervals (CIs).

II. METHOD

A. Effective-One-Body Waveforms

We compute eccentric (and non-spinning) BNS signals using **TEOBResumS-Dalí** [40] (see also [27, 40, 42] for details), a unified EOB approximant for the general relativistic dynamics and gravitational radiation of generic compact binaries. When describing BNSs, the conservative Hamiltonian of **TEOBResumS-Dalí** incorporates point mass information up to 5PN [43]. Spin-orbit contributions are instead included at next-to-next-to-leading order (NNLO) [28, 44], and inverse-resummed following the EOB prescriptions detailed in Ref. [43]. Finally, even-in-spin effects are accounted for up to NNLO via the centrifugal radius. The radiative sector contains orbital contributions at 3^{+2} PN order – meaning that 3PN terms are integrated by 4PN and 5PN test-particle terms – and spin-spin interaction at next-to-leading order (NLO) for the $(2, 2)$ mode and leading order (LO) for the $(2, 1), (3, 1)$ and $(3, 3)$ modes.

Within **TEOBResumS-Dalí**, the initial eccentricity e_0 and the initial orbit-averaged frequency f_0 determine the initial conditions of the (Hamiltonian) equations of motion via

$$r_0 = \frac{p_0}{1 + e_0 \cos \zeta_0}, \quad (8)$$

where r_0 is the initial separation of the binary components, p_0 is the semi-latus rectum of the orbit (which itself is a function of f_0 and e_0) and ζ_0 is the initial true anomaly, in all cases considered set to π . After initial conditions are determined, the EOB model evolves the system under the influence of GW radiation reaction, which includes non-circular effects in its azimuthal component via the prescription described in App. A of Ref. [45], and employs a non-zero radial component [27].

Inference (or recovery) is performed with the quasi-circular (non-eccentric) version of that model, which is consistent with **TEOBResumS-GIOTTO** [43, 46–48], and shares the same conservative dynamics and equations

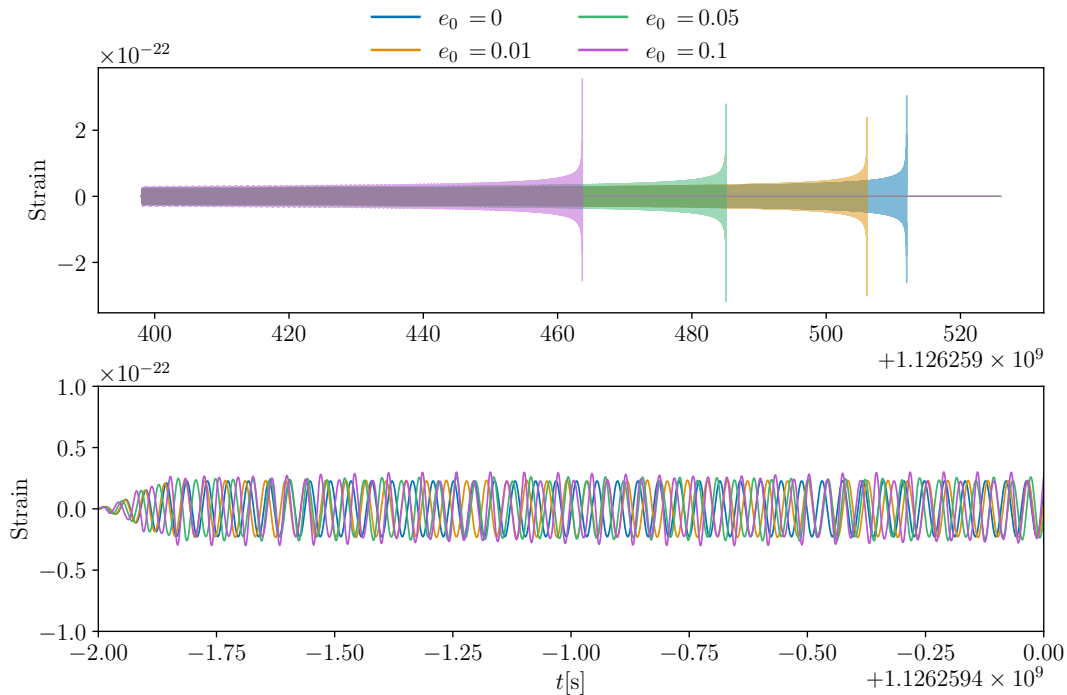


FIG. 1. Injected waveforms for different values of eccentricity, as reported in the legend. The injections have been performed with **TEOBResumS-Da1i** model, with $\mathcal{M} = 1.1977 M_{\odot}$, $q = 1.5$, $\Lambda_1 = 400$, $\Lambda_2 = 600$, $D_L = 40$ Mpc and $\iota = 45^\circ$.

of motions (EOMs) as **TEOBResumS-Da1i**. The crucial difference is that no radial radiation reaction force and non-circular effects are included in the description of the GW flux and multipoles. Both EOB models provide a faithful description of tidal effects up to merger [49, 50] and include spin precessional effects [51]. For non eccentric binaries, **TEOBResumS** implements the post-adiabatic approximation for the solution of the Hamilton equations [52] and the EOB-SPA method to efficiently obtain frequency-domain waveforms [53]. Both methods are key to speed-up the generation of long BNS waveforms.

B. Bayesian Parameter Estimation

The PE experiments of this work are performed by injecting eccentric BNS signals and recovering them with a full Bayesian analysis that employs the quasi-circular model described above. The Bayesian analyses are performed with the MPI-parallelized **bajes** pipeline [54]. The Bayesian framework and the setup is summarized in what follows. We refer to Ref. [55, 56] for a detailed discussion on Bayesian inference.

In the context of GW data analysis, the matched-filtered SNR of a template $h(t)$ with respect to the data $d(t)$ is

$$\rho := \frac{(d|h)}{\sqrt{(h|h)}}, \quad (9)$$

where the inner product between two time series $a(t)$ and $b(t)$ is defined in the frequency space by

$$(a|b) := \int \frac{\tilde{a}^*(f)\tilde{b}(f)}{S_n(f)} df, \quad (10)$$

with $S_n(f)$ the power spectral density (PSD) of the noise segment. For multiple detectors, Eq. (9) can be generalized employing the sum in quadrature.

The inner product of Eq. (10) forms also the basis for the likelihood function $p(d|h(\boldsymbol{\theta}), H)$,

$$\log p(d|h(\boldsymbol{\theta}), H) \propto -\frac{1}{2} \sum_i (d - h(\boldsymbol{\theta})|d - h(\boldsymbol{\theta}))_i, \quad (11)$$

where H represents the signal hypothesis, the subscript i runs over the employed detectors and the parameter vector $\boldsymbol{\theta}$ corresponds to the combination of the BNS parameters we infer. Due to the complexity and the multidimensionality of the likelihood function, we employ nested sampling algorithms [57–59] to estimate the posterior $p(\boldsymbol{\theta}|d, H)$ and the evidence $Z = p(d, H)$, obtained by integrating the likelihood over the prior distribution of the model parameters.

The injected GW signals correspond to non-spinning eccentric BNS with $\mathcal{M} = 1.1977 M_{\odot}$ (in the detector frame), $q = 1.5$, $\Lambda_1 = 400$ and $\Lambda_2 = 600$ ($\tilde{\Lambda} = 488$ and $\delta\tilde{\Lambda} = -60$). The considered eccentricity values are

$$e_0 = (0, 0.01, 0.05, 0.1). \quad (12)$$

Mock GW data are generated for the LIGO-Virgo three-detector network [60–64] with a duration of 128 s and a sampling rate of 4096 Hz. Each signal is injected with inclination angle $\iota = 45^\circ$ at different distances,

$$D_L = (40, 80, 100) \text{ Mpc}. \quad (13)$$

The injections (See Fig. 1) are performed with both zero-noise or using Gaussian-and-stationary noise colored according to the PSDs of the GW170817 event [63]. The injected signals span the range of SNRs $\rho_{\text{inj}} \in [12, 32]$. The total number of mock GW data (and thus PE experiments) is $4 \times 3 \times 2 = 24$.

Our Bayesian PE analyses employ the nested sampling implementation of `dynesty` [65] with a minimum of 3000 live points as baseline (used for most of the simulations). The likelihood is computed over the frequency range from 23 Hz to 2000 Hz employing the GW170817 PSDs [63] and it is marginalized over reference time and phase. Therefore, the sampling explores a 15-dimensional parameters space,

$$\theta = \{m_1, m_2, \vec{\chi}_1, \vec{\chi}_2, \Lambda_1, \Lambda_2, D_L, \iota, \alpha, \delta, \psi\}, \quad (14)$$

where (α, δ) identify the sky position of the source (right ascension and declination respectively) and $\psi \in [0, \pi]$ is the polarization angle. The prior follows closely the standard choices described in [54] with isotropic spins and volumetric luminosity distance. The prior bounds are chosen as follows:

$$\mathcal{M} \in [1, 1.5], \quad (15a)$$

$$q \leq q_{\text{max}} = (4, 10, 50), \quad (15b)$$

$$|\vec{\chi}_i| \leq 0.9, \quad (15c)$$

$$\Lambda_i \in [0, 5000], \quad (15d)$$

$$D_L \in [10, 500] \text{ Mpc}. \quad (15e)$$

The prior on the mass ratio has $q_{\text{max}} = 10$ for most of the simulations but some simulations have considered the other values as described below.

In the case of zero-noise injections we performed the inference both using aligned and precessing spins priors.

III. RESULTS

The results of our analysis are discussed in the following, starting from the non-precessing and moving to the precessing case. In either scenario we study the recovered SNR and the biases in the source parameters. In this section e always refers to the eccentricity at $f_0 = 23 \text{ Hz}$ (*i.e.* e_0).

A. Non-precessing inferences

In this subsection we discuss the results obtained when inference is performed with quasi-circular non-precessing

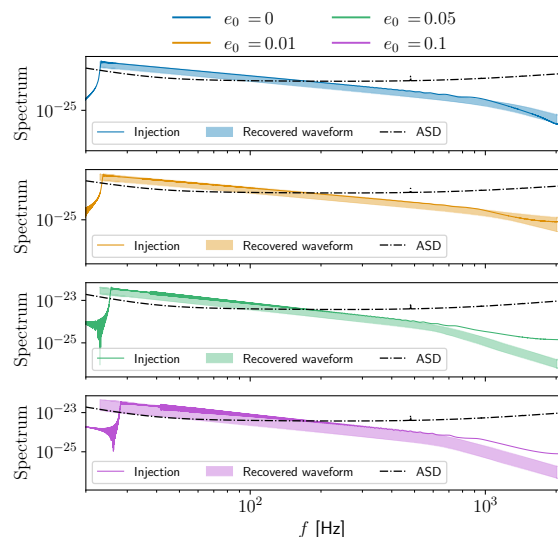


FIG. 2. Injected and reconstructed waveforms in the spin-aligned case for different values of eccentricity, as reported in the legend. The injections, plotted with solid lines, have been performed with `TEOBResumS-Da11` model, with $\mathcal{M} = 1.1977 M_\odot$, $q = 1.5$, $\Lambda_1 = 400$, $\Lambda_2 = 600$, $D_L = 40 \text{ Mpc}$ and $\iota = 45^\circ$. The shaded regions are the 90% credibility regions of the reconstructed spectrum and the dash-dotted line represents the ASD of GW170817 event.

waveforms. The results for both Gaussian and zero-noise are collected in Tab. I.

Examples of the recovered waveforms in frequency domain are shown in Fig. 2. The figure suggests that the most informative portion of the signals is up to $\sim 200 \text{ Hz}$ [66]. In this frequency range, the injected data (solid lines) appear well reproduced by the best quasi-circular waveform (colored region, corresponding to 90% CI); the agreement worsens for the largest simulated eccentricities which are clearly not contained within the 90% CIs. At higher frequencies the merger waveform is captured only for the smallest eccentricity and for the non-eccentric binary, while the other two recoveries predict an earlier merger than the injection. This qualitative analysis already suggests that the chirp mass inferred from early frequencies overestimates the injected one.

Figure 3 summarizes the loss of matched-filtered SNR due to the use of the quasi-circular spin-aligned templates in the analyses of the eccentric signals. We define the SNR loss $\Delta\rho = \rho_{\text{inj}} - \rho_{\text{rec}}$ as the difference between the SNR of the injected template ρ_{inj} and the SNR recovered with quasi-circular template ρ_{rec} . The SNR loss increases with the eccentricity, raising from $\sim 2\%$ for $e = 0.01$ to $\sim 25\%$ for $e = 0.1$.

If we consider the maximum value of the matched-filtered SNR (diamond markers) instead of the median one (round markers), the SNR loss decreases to $\sim 0.5\%$ for $e = 0.01$ to $\sim 20\%$ for $e = 0.1$. This is due to the fact that, in the case of zero-noise, the maximum value of

TABLE I. Summary table, spin-aligned PEs.

| Injected properties | | | | | | Recovered properties | | | | | |
|---------------------|---|----------------|---------------------|------------------|-------|----------------------------------|------------------------|----------------------------|------------------------|--------------------|-------------------------|
| e | \mathcal{M}_{ecc} [M_{\odot}] | D_L [Mpc] | ρ_{inj} | q_{max} | Noise | \mathcal{M} [M_{\odot}] | q | χ_{eff} | $\tilde{\Lambda}$ | D_L [Mpc] | ρ_{rec} |
| 0 | 1.1977 | 40 | 31.7 | 4 | Z | $1.1977^{+0.0003}_{-0.0002}$ | $1.48^{+0.65}_{-0.41}$ | $0.003^{+0.066}_{-0.029}$ | 573^{+455}_{-319} | 36^{+19}_{-12} | $31.05^{+0.59}_{-0.57}$ |
| | | 80 | 15.9 | 4 | Z | $1.1979^{+0.0006}_{-0.0003}$ | $1.52^{+1.05}_{-0.45}$ | $0.016^{+0.118}_{-0.038}$ | 1046^{+1849}_{-864} | 78^{+57}_{-32} | $15.38^{+0.32}_{-0.46}$ |
| | | 100 | 12.7 | 4 | Z | $1.1979^{+0.0007}_{-0.0004}$ | $1.46^{+1.14}_{-0.40}$ | $0.015^{+0.134}_{-0.037}$ | 1443^{+2286}_{-1139} | 105^{+72}_{-52} | $12.21^{+0.33}_{-0.49}$ |
| 0.01 | 1.982 | 40 | 31.7 | 10 | Z | $1.1980^{+0.0004}_{-0.0002}$ | $1.60^{+0.91}_{-0.50}$ | $0.023^{+0.091}_{-0.040}$ | 623^{+546}_{-414} | 37^{+19}_{-13} | $31.02^{+0.58}_{-0.59}$ |
| | | 80 | 15.9 | 10 | Z | $1.1981^{+0.0006}_{-0.0003}$ | $1.53^{+1.09}_{-0.45}$ | $0.024^{+0.124}_{-0.037}$ | 1116^{+1838}_{-878} | 75^{+53}_{-33} | $15.37^{+0.32}_{-0.48}$ |
| | | 100 | 12.7 | 10 | Z | $1.1982^{+0.0008}_{-0.0004}$ | $1.54^{+1.11}_{-0.46}$ | $0.032^{+0.153}_{-0.047}$ | 1520^{+2370}_{-1230} | 110^{+69}_{-54} | $12.21^{+0.31}_{-0.52}$ |
| 0.05 | 1.2096 | 40 | 31.6 | 10 | Z | $1.2091^{+0.0013}_{-0.0014}$ | $9.23^{+0.69}_{-1.87}$ | $0.652^{+0.090}_{-0.080}$ | 120^{+98}_{-58} | 38^{+18}_{-13} | $28.99^{+0.45}_{-0.47}$ |
| | | 80 | 15.8 | 10 | Z | $1.2076^{+0.0040}_{-0.0044}$ | $6.93^{+2.90}_{-5.31}$ | $0.604^{+0.206}_{-0.326}$ | 249^{+3936}_{-178} | 89^{+39}_{-47} | $14.28^{+0.28}_{-0.47}$ |
| | | 100 | 12.6 | 10 | Z | $1.2057^{+0.0060}_{-0.0033}$ | $4.14^{+5.71}_{-2.81}$ | $0.522^{+0.287}_{-0.338}$ | 750^{+3947}_{-641} | 114^{+65}_{-56} | $11.30^{+0.31}_{-0.59}$ |
| 0.1 | 1.2473 | 40 | 31.4 | 10 | Z | $1.2197^{+0.0018}_{-0.0013}$ | $9.24^{+0.70}_{-1.60}$ | $0.829^{+0.069}_{-0.050}$ | 94^{+52}_{-22} | 53^{+20}_{-20} | $24.12^{+0.47}_{-0.59}$ |
| | | 80 | 15.7 | 10 | Z | $1.2127^{+0.0064}_{-0.0036}$ | $2.47^{+6.72}_{-1.35}$ | $0.587^{+0.225}_{-0.271}$ | 1015^{+3118}_{-950} | 117^{+66}_{-55} | $11.67^{+0.41}_{-0.64}$ |
| | | 100 | 12.6 | 10 | Z | $1.2113^{+0.0066}_{-0.0037}$ | $1.75^{+5.41}_{-0.68}$ | $0.449^{+0.298}_{-0.218}$ | 1419^{+2776}_{-1361} | 160^{+103}_{-83} | $9.05^{+0.49}_{-0.71}$ |
| 0 | 1.1977 | 40 | 33.9 | 4 | G | $1.1977^{+0.0002}_{-0.0001}$ | $1.40^{+0.55}_{-0.33}$ | $-0.007^{+0.054}_{-0.021}$ | 587^{+275}_{-301} | 36^{+16}_{-14} | $33.20^{+0.75}_{-0.78}$ |
| | | 80 | 14.5 | 4 | G | $1.1980^{+0.0006}_{-0.0003}$ | $1.42^{+1.08}_{-0.37}$ | $0.013^{+0.121}_{-0.032}$ | 1256^{+2016}_{-894} | 83^{+48}_{-38} | $14.43^{+0.56}_{-0.55}$ |
| | | 100 | 12.0 | 4 | G | $1.1981^{+0.0007}_{-0.0005}$ | $1.51^{+1.18}_{-0.44}$ | $0.026^{+0.137}_{-0.049}$ | 2397^{+1909}_{-1821} | 102^{+70}_{-65} | $12.32^{+0.36}_{-0.57}$ |
| 0.01 | 1.1982 | 40 | 32.9 | 4 | G | $1.1980^{+0.0004}_{-0.0002}$ | $1.45^{+0.79}_{-0.39}$ | $0.009^{+0.086}_{-0.027}$ | 641^{+648}_{-313} | 40^{+16}_{-18} | $32.16^{+0.67}_{-0.64}$ |
| | | 80 | 17.5 | 4 | G | $1.1981^{+0.0006}_{-0.0003}$ | $1.48^{+1.05}_{-0.41}$ | $0.019^{+0.130}_{-0.038}$ | 1101^{+2101}_{-884} | 66^{+43}_{-30} | $17.22^{+0.34}_{-0.47}$ |
| | | 100 | 12.4 | 4 | G | $1.1983^{+0.0007}_{-0.0005}$ | $1.43^{+1.04}_{-0.38}$ | $0.030^{+0.131}_{-0.040}$ | 1472^{+1814}_{-1094} | 98^{+63}_{-52} | $12.20^{+0.47}_{-0.56}$ |
| 0.05 | 1.2096 | 40 | 30.6 | 4 | G | $1.2063^{+0.0026}_{-0.0014}$ | $3.60^{+0.39}_{-1.43}$ | $0.625^{+0.267}_{-0.157}$ | 1600^{+2633}_{-555} | 49^{+13}_{-23} | $28.13^{+0.42}_{-0.47}$ |
| | | 80 | 16.0 | 4 | G | $1.2044^{+0.0030}_{-0.0021}$ | $2.38^{+1.53}_{-1.20}$ | $0.387^{+0.265}_{-0.235}$ | 1733^{+2595}_{-1201} | 81^{+48}_{-37} | $14.83^{+0.35}_{-0.53}$ |
| | | 100 | 13.5 | 4 | G | $1.2038^{+0.0035}_{-0.0016}$ | $2.05^{+1.83}_{-0.88}$ | $0.345^{+0.330}_{-0.203}$ | 2954^{+2434}_{-2310} | 94^{+66}_{-58} | $12.66^{+0.35}_{-0.47}$ |
| 0.1 | 1.2473 | 40 | 31.6 | 10 | G | $1.2185^{+0.0008}_{-0.0010}$ | $8.67^{+1.14}_{-1.88}$ | $0.800^{+0.039}_{-0.039}$ | 104^{+77}_{-30} | 52^{+19}_{-20} | $25.21^{+0.50}_{-0.51}$ |
| | | 80 | 14.5 | 10 | G | $1.2076^{+0.0113}_{-0.0013}$ | $1.97^{+7.29}_{-0.85}$ | $0.355^{+0.438}_{-0.162}$ | 2137^{+2378}_{-2059} | 108^{+63}_{-51} | $12.20^{+0.41}_{-0.55}$ |
| | | 100 | 12.2 | 10 | G | $1.2091^{+0.0019}_{-0.0009}$ | $1.44^{+1.60}_{-0.40}$ | $0.318^{+0.207}_{-0.091}$ | 2374^{+1604}_{-1911} | 140^{+89}_{-66} | $9.79^{+0.44}_{-0.62}$ |

the SNR achievable is the injected one, since there is no noise that can shift the peak of the distribution to larger values. Furthermore, using the maximum values of the SNR, the relative SNR loss $\Delta\rho/\rho_{\text{inj}}$ is almost independent on the injected SNR ρ_{inj} . Hence, for the considered SNR and eccentricity ranges, we find that the SNR loss can be fit to

$$\frac{\Delta\rho}{\rho_{\text{inj}}} \approx \alpha e, \quad (16)$$

with $\alpha = 2.27 \pm 0.17^1$. Notably, these results are rather independent on the noise realization for $e \lesssim 0.05$, as the

variations of $\Delta\rho/\rho_{\text{inj}}$ for the Gaussian noise simulations (triangular markers) are in agreement with the fits for zero-noise.

The most prominent feature of the posteriors is the bias in the chirp mass parameter. Figure 4 shows the recovered chirp masses and mass ratios for the injections at $D_L = 40, 100$ Mpc (zero-noise). All the posteriors of the chirp mass are systematically shifted to larger median values as the eccentricity increases. This bias can be interpreted with a Newtonian argument [23]. Chirp mass and eccentricity enter the leading order expression of the waveform's phase via the combination

$$\mathcal{M}_{\text{ecc}} = \mathcal{M} \left(1 - \frac{157}{24} e^2 \right)^{-3/5}. \quad (17)$$

The above expression is valid for small eccentricities and low frequencies. Since the quasi-circular templates have

¹ In order to reduce the impact of noise fluctuations, the presented relation is calibrated only on zero-noise results.

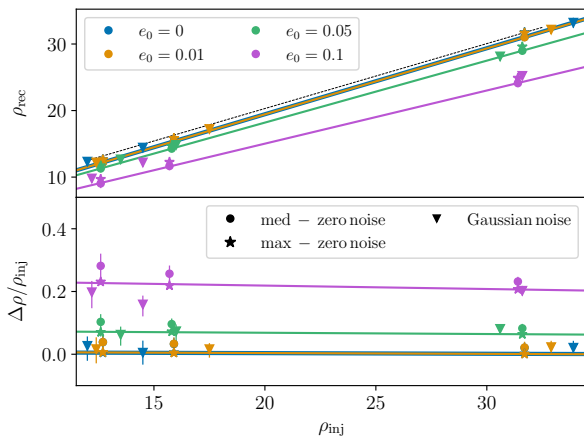


FIG. 3. Recovered SNR (top panel) and SNR loss (bottom panel) as function of the injected SNR for spin-aligned PEs. Different colors refer to different eccentricities as reported in the legend. Round markers show the results of the median values of matched-filtered SNR, star markers of the maximum values of the SNR, both for zero-noise case, whereas triangular markers show the median values of the SNR in the case of Gaussian noise.

$e = 0$, the eccentric signal can only be reproduced with a larger \mathcal{M} . Figure 5 and Tab. I show that the recovered \mathcal{M} are consistent with the values predicted by Eq. (17) within the 90% confidence level up to eccentricity $e = 0.05$ in the case of zero-noise. For the $e = 0.1$ cases, the recovered values are smaller than the prediction of Eq. (17). This means that Eq. (17) is not accurate to quantitatively predict the biases for eccentricities $e > 0.05$.

From Fig. 4 we can also comment about the mass ratio. For zero and small eccentricity $e = 0.01$ the mass ratio is compatible with the injected value. The mass ratio inference is found significantly biased and strongly degenerate with the chirp mass for $e \gtrsim 0.05$. In all the analyses with $e \gtrsim 0.05$ and $q_{\max} = 4$ or $q_{\max} = 10$ the mass ratio posteriors systematically rails against the q_{\max} prior and, for the smallest luminosity distance considered, the posteriors are sufficiently narrow to not support the injected value anymore.

This effect is further investigated in the case of $e = 0.05$ and $D_L = 40$ Mpc by means of (i) a PE run with $q_{\max} = 10$ with increasing the live point of the sampler to 5000, in order to test convergence; and (ii) a PE run with $q_{\max} = 50$ (3000 live points). The first simulation shows again that the q -posterior is railing against its upper bound. This suggests that this effect is not due to the sampler. The second simulation returns a converged posterior peaked at $q = 22 \pm 5$. The posteriors of this run are shown in Fig. 6. This run also yields a chirp mass larger than \mathcal{M}_{ecc} from Eq. (17). In a real PE the single object masses would be inferred as $m_1 \approx 8 M_\odot$ and $m_2 \approx 0.35 M_\odot$, neither of which can be identified as a NS object. The reduced tidal parameter inferred by this

run is $\tilde{\Lambda} = 4.00^{+3.99}_{-1.81}$ that, together with the single object masses, yields $\Lambda_1 = 2.57^{+2.52}_{-1.16}$ and $\Lambda_2 = 1553^{+2256}_{-988}$. While the heavier binary component would be misidentified as a black hole (BH) the secondary would be identified neither as a NS nor a BH.

Figure 7 shows the posterior distributions of mass ratio and effective spin χ_{eff} for $D_L = 40$ Mpc. The signal at $e = 0.01$ is marginally compatible with the zero spin at 90% CI (see Tab. I), while significant biases are present already at $e = 0.05$. Similar to the chirp mass, the effective spin parameter is progressively more biased for signal from larger eccentricities and at close distances. All the inferences of eccentric BNSs deliver a positive χ_{eff} . Since the template we are using for the analysis does not include eccentricity, the PE returns a larger value of χ_{eff} to compensate the eccentric effects in the form of spin-orbit interactions.

Finally, Fig. 8 shows the posteriors of the tidal parameters for $D_L = 40$ Mpc. The posteriors capture the correct value of $\tilde{\Lambda}$ within the statistical accuracy expected at these SNR for sufficiently small eccentricities $e \sim 0.01$. For comparison, the eccentricities inferred in [11] for GW170817 are a factor two-to-four larger. At larger eccentricities $e \gtrsim 0.05$ the reduced tidal parameter is biased towards significantly smaller values. This parameter is also degenerate with the mass ratio: large values of q usually moves the peak of the reduced tidal parameters posterior close to zero for small distances. Combined with the bias in the chirp mass and mass ratio, this can lead to an incorrect (and puzzling) interpretation of the source as discussed above.

The PEs relative to injections with Gaussian noise are generally consistent with the zero-noise ones, as reported in Table I. For $e = 0$ and $e = 0.01$ all the recovered values are coherent with our injections, except the chirp mass in the eccentric case, since the eccentricity is taken into account in \mathcal{M}_{ecc} (Eq. (17)). At higher eccentricities $e \gtrsim 0.05$ the mass ratio is railing against the prior and the chirp mass is larger than the injected value, but smaller than what is expected from Eq. (17). The effective spins are not compatible with the non-spinning injected values, as a compensation of the eccentricity, which is not considered in our recovery model with the quasi-circular template. As the eccentricity increases, the values of the tidal polarizability parameters are incompatible with the injected ones and we notice a loss in the SNR, similar to the zero-noise case.

B. Spin Precession

In this subsection we discuss the results obtained when inference is performed with quasi-circular precessing waveforms. The results are collected in Tab. II. Since in the previous subsection we observed that the Gaussian noise cases are similar to the zero-noise ones, we present here only the zero-noise PEs.

Figure 9 shows the posterior distributions of chirp

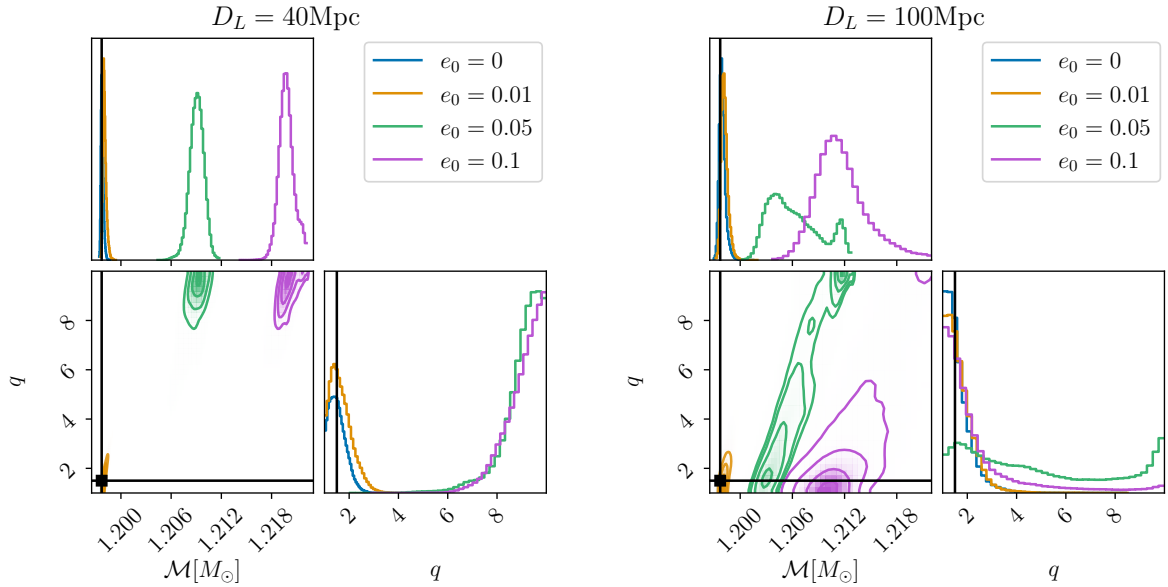


FIG. 4. Posterior distribution of chirp masses and mass ratios for spin-aligned PEs with zero noise, for two different luminosity distances $D_L = 40$ Mpc ($\rho_{\text{inj}} = 31.7$) and $D_L = 100$ Mpc ($\rho_{\text{inj}} = 12.7$). Injected values are identified by the black lines.

TABLE II. Summary table, spin-precessing PEs

| Injected properties | | | | | | Recovered properties | | | | | | |
|---------------------|---|----------------|---------------------|------------------|-------|----------------------------------|------------------------|---------------------------|---------------------------|------------------------|--------------------|-------------------------|
| e | \mathcal{M}_{ecc} [M_{\odot}] | D_L [Mpc] | ρ_{inj} | q_{max} | Noise | \mathcal{M} [M_{\odot}] | q | χ_{eff} | χ_p | $\tilde{\Lambda}$ | D_L [Mpc] | ρ_{rec} |
| 0 | 1.1977 | 40 | 31.7 | 4 | Z | $1.1978^{+0.0004}_{-0.0002}$ | $1.59^{+0.82}_{-0.49}$ | $0.014^{+0.083}_{-0.039}$ | $0.211^{+0.440}_{-0.183}$ | 546^{+538}_{-389} | 40^{+16}_{-15} | $31.11^{+0.52}_{-0.62}$ |
| | | 80 | 15.9 | 4 | Z | $1.1979^{+0.0005}_{-0.0003}$ | $1.53^{+1.04}_{-0.48}$ | $0.013^{+0.107}_{-0.039}$ | $0.286^{+0.432}_{-0.230}$ | 1091^{+1980}_{-872} | 82^{+43}_{-37} | $15.37^{+0.34}_{-0.47}$ |
| | | 100 | 12.7 | 4 | Z | $1.1979^{+0.0006}_{-0.0004}$ | $1.56^{+1.12}_{-0.50}$ | $0.022^{+0.117}_{-0.046}$ | $0.325^{+0.453}_{-0.267}$ | 1521^{+2253}_{-1250} | 105^{+65}_{-48} | $12.19^{+0.30}_{-0.51}$ |
| 0.01 | 1.1982 | 40 | 31.7 | 10 | Z | $1.1981^{+0.0004}_{-0.0002}$ | $1.78^{+0.70}_{-0.65}$ | $0.037^{+0.082}_{-0.052}$ | $0.308^{+0.331}_{-0.226}$ | 604^{+645}_{-382} | 41^{+13}_{-16} | $30.99^{+0.59}_{-0.63}$ |
| | | 80 | 15.8 | 10 | Z | $1.1981^{+0.0006}_{-0.0004}$ | $1.56^{+1.26}_{-0.49}$ | $0.027^{+0.123}_{-0.044}$ | $0.296^{+0.419}_{-0.228}$ | 1140^{+2121}_{-920} | 81^{+43}_{-33} | $15.34^{+0.32}_{-0.47}$ |
| | | 100 | 12.7 | 10 | Z | $1.1981^{+0.0007}_{-0.0004}$ | $1.52^{+1.24}_{-0.47}$ | $0.027^{+0.122}_{-0.045}$ | $0.312^{+0.433}_{-0.252}$ | 1769^{+2354}_{-1449} | 103^{+64}_{-44} | $12.18^{+0.30}_{-0.46}$ |
| 0.05 | 1.2096 | 40 | 31.6 | 10 | Z | $1.2093^{+0.0012}_{-0.0017}$ | $9.00^{+0.88}_{-2.08}$ | $0.668^{+0.079}_{-0.098}$ | $0.211^{+0.152}_{-0.138}$ | 141^{+132}_{-70} | 44^{+13}_{-15} | $29.02^{+0.48}_{-0.49}$ |
| | | 80 | 15.8 | 10 | Z | $1.2071^{+0.0035}_{-0.0041}$ | $5.73^{+4.07}_{-4.21}$ | $0.579^{+0.168}_{-0.343}$ | $0.297^{+0.303}_{-0.203}$ | 383^{+4362}_{-304} | 92^{+37}_{-38} | $14.31^{+0.28}_{-0.51}$ |
| | | 100 | 12.6 | 10 | Z | $1.2042^{+0.0056}_{-0.0021}$ | $2.31^{+6.94}_{-1.14}$ | $0.376^{+0.319}_{-0.233}$ | $0.375^{+0.331}_{-0.251}$ | 2918^{+2385}_{-2790} | 120^{+69}_{-57} | $11.29^{+0.30}_{-0.55}$ |
| 0.1 | 1.2473 | 40 | 31.7 | 10 | Z | $1.2194^{+0.0013}_{-0.0017}$ | $9.11^{+0.83}_{-2.41}$ | $0.817^{+0.044}_{-0.051}$ | $0.196^{+0.149}_{-0.132}$ | 95^{+95}_{-21} | 49^{+25}_{-22} | $24.06^{+0.49}_{-0.55}$ |
| | | 80 | 15.7 | 10 | Z | $1.2119^{+0.0058}_{-0.0029}$ | $1.60^{+6.85}_{-0.54}$ | $0.504^{+0.248}_{-0.211}$ | $0.412^{+0.287}_{-0.270}$ | 2643^{+1814}_{-2567} | 114^{+77}_{-56} | $11.69^{+0.38}_{-0.59}$ |
| | | 100 | 12.6 | 10 | Z | $1.2113^{+0.0066}_{-0.0037}$ | $1.75^{+5.41}_{-0.68}$ | $0.449^{+0.298}_{-0.218}$ | $0.421^{+0.286}_{-0.277}$ | 1419^{+2776}_{-1361} | 160^{+103}_{-83} | $9.12^{+0.43}_{-0.64}$ |

masses and mass ratios for $D_L = 40, 100$ Mpc. As in the aligned case we note that the chirp mass posteriors are shifted to larger values as the eccentricity increases and the values are compatible with \mathcal{M}_{ecc} (Eq.(17)) for $e \lesssim 0.05$.

The mass ratio has again the most significant bias for the eccentric BNSs, as shown in Fig. 9. For the smallest luminosity distance ($D_L = 40$ Mpc) and $e \gtrsim 0.05$, we obtain values of the mass ratio $\gtrsim 9$. For the largest luminosity distance, *i.e.* the smaller SNR, the injected values are instead compatible with the recovered ones

within the 90% CI, meaning that there is a threshold SNR from which we start observing the biases.

The effective spin is progressively biased for larger eccentricities, as for the spin-aligned case. The spin precessing parameter, whose posterior distribution are reported in Figure 10 together with the effective one at $D_L = 40, 100$ Mpc, is not well constrained. We stress again that the template we are using for the inference is quasi-circular, therefore the influence of the eccentricity is taken into account as spin-orbit effects, leading to the increase of the effective spin for $e \gtrsim 0.05$.

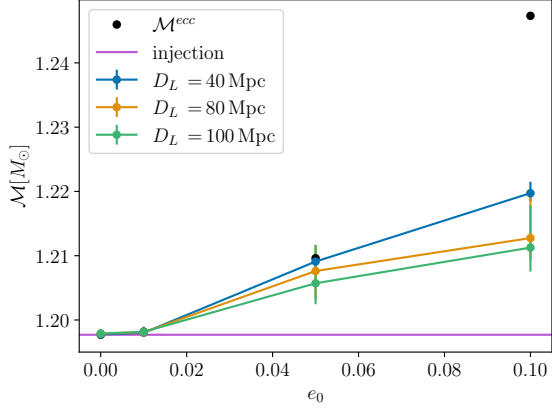


FIG. 5. Recovered \mathcal{M} as function of the eccentricity for spin-aligned PEs. Different colors refer to different injection distances as reported in the legend. The black dots show the leading order approximation for \mathcal{M}_{ecc} as per Eq. (17)

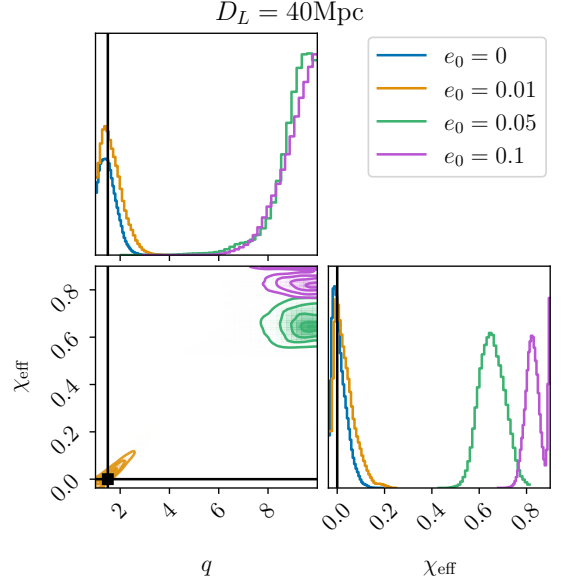


FIG. 7. Posterior distribution of effective spin parameters and mass ratios for spin-aligned PEs with zero-noise for $D_L = 40$ Mpc ($\rho_{\text{inj}} = 31.7$). Injected values are identified by the black lines.

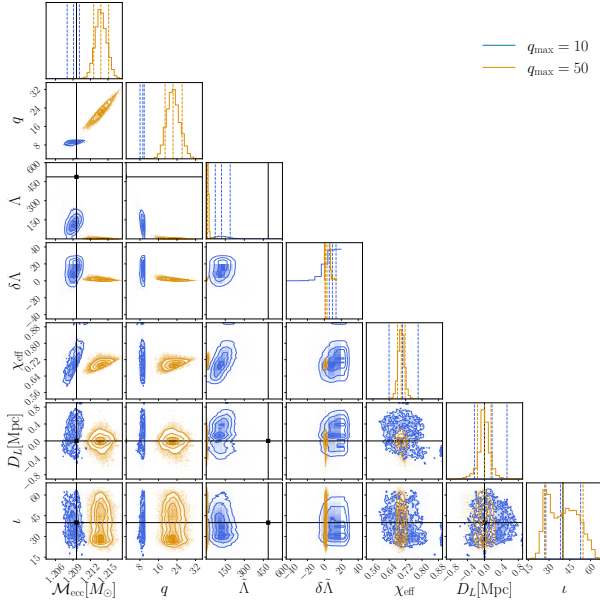


FIG. 6. Corner plot for the $e = 0.05$, $D_L = 40$ Mpc ($\rho_{\text{inj}} = 31.6$) spin-aligned configuration with an upper bound for the mass ratio of $q_{\text{max}} = 50$ (yellow) and $q_{\text{max}} = 10$ (blue). The black lines mark the injected values.

Figure 11 shows the posterior distributions of the tidal polarizability parameters for $D_L = 40$ Mpc, again the result is in accordance with the spin-aligned case: at higher eccentricities $\tilde{\Lambda}$ is underestimated.

In Figure 12 we report the SNR loss for the quasi-circular spin-precession analysis. Similar to the spin-aligned case, as the eccentricity increases, the difference between the injected and the recovered SNR increases, for $e = 0.01$ is $\sim 2\%$, whereas for $e = 0.1$ it reaches $\sim 25\%$. Since the results are comparable with the case of spin-aligned PEs, we can conclude that the eccentricity

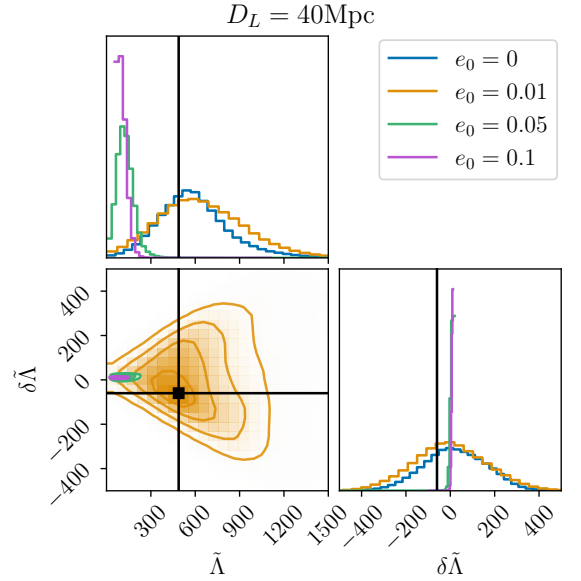


FIG. 8. Posterior distributions of tidal polarizability parameters and asymmetric tidal parameters for spin-aligned PEs with zero-noise for $D_L = 40$ Mpc ($\rho_{\text{inj}} = 31.7$). Injected values are identified by the black lines.

is not mimicked by the precession.

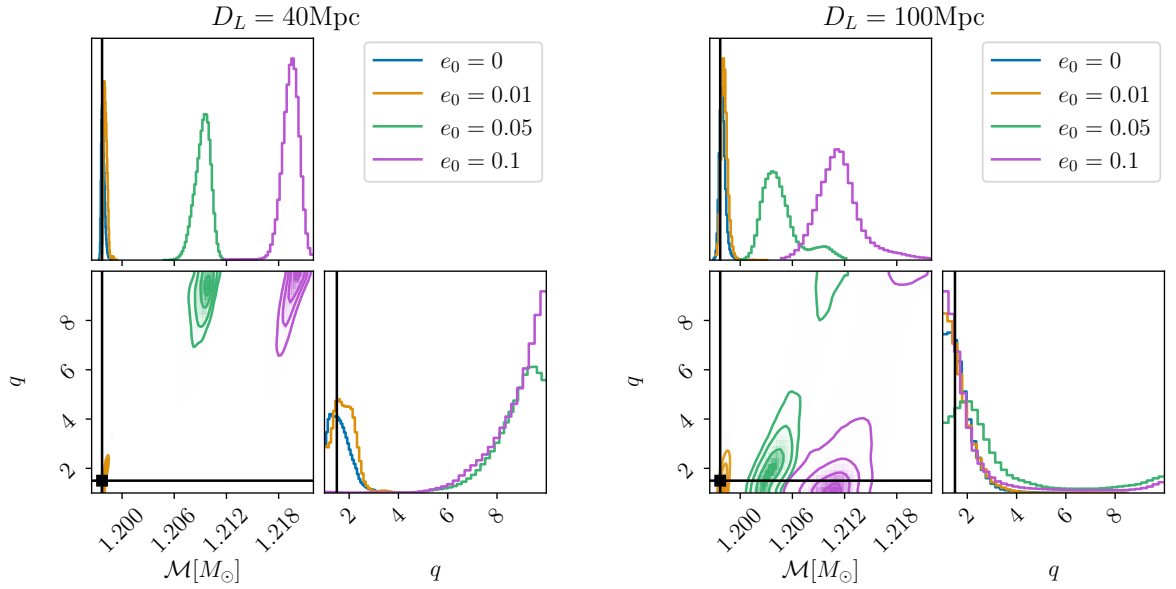


FIG. 9. Posterior distributions of chirp masses and mass ratios for spin-precessing PEs for two different luminosity distances $D_L = 40 \text{ Mpc}$ ($\rho_{\text{inj}} = 31.7$) and $D_L = 100 \text{ Mpc}$ ($\rho_{\text{inj}} = 12.7$). Injected values are identified by the black lines.

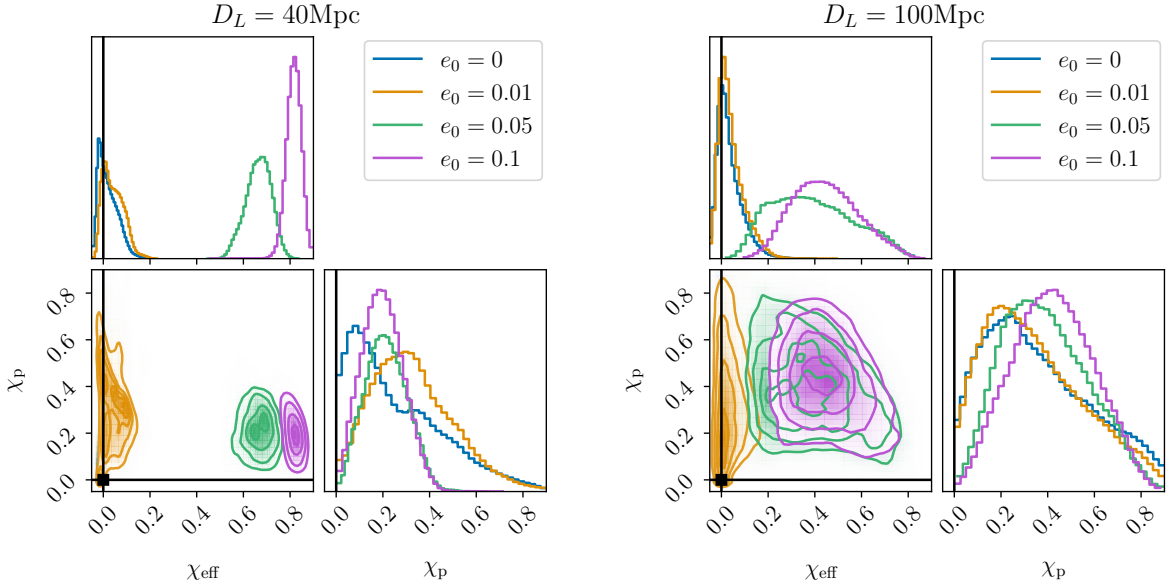


FIG. 10. Posterior distributions of the parallel effective and perpendicular spins for spin-precessing PEs for two different luminosity distances $D_L = 40 \text{ Mpc}$ ($\rho_{\text{inj}} = 31.7$) and $D_L = 100 \text{ Mpc}$ ($\rho_{\text{inj}} = 12.7$). Injected values are identified by the black lines.

IV. CONCLUSIONS

In this paper we demonstrated that use of quasi-circular and spinning BNS waveforms in Bayesian inference of eccentric BNS signals with $e_0 \gtrsim 0.05$ can lead to significant parameter biases already at $\text{SNR} \gtrsim 12$. In our experiments several key parameters are profoundly affected by the use (assumption) of a non-eccentric wave-

form. Biases in the chirp mass and mass ratio can be so severe to affect the source interpretation: in the worst case the BNS signal would be associated to a binary composed of a $\sim 8 M_\odot$ black hole and a sub-solar mass compact object incompatible with a NS. The biases in the chirp mass and mass ratio reflect on the inference of the reduced tidal parameters which, in the considered experiment, is significantly underestimated. This would have obvious consequences for inference of the NS mat-

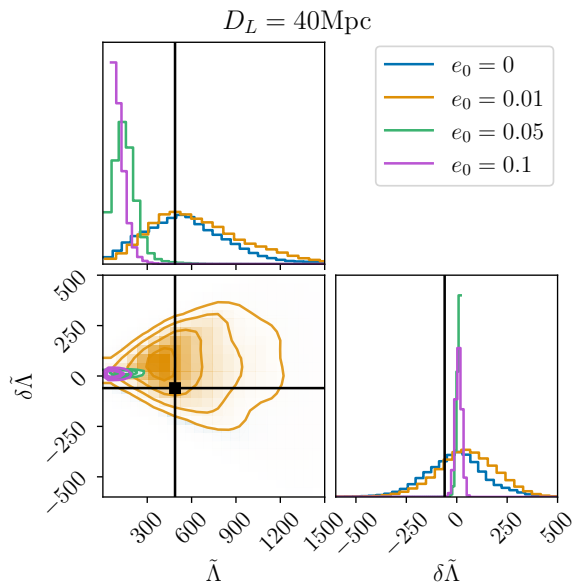


FIG. 11. Posterior distributions of tidal polarizability parameters and asymmetric tidal parameters for spin-precessing PEs for $D_L = 40$ Mpc ($\rho_{\text{inj}} = 31.7$). Injected values are identified by the black lines.

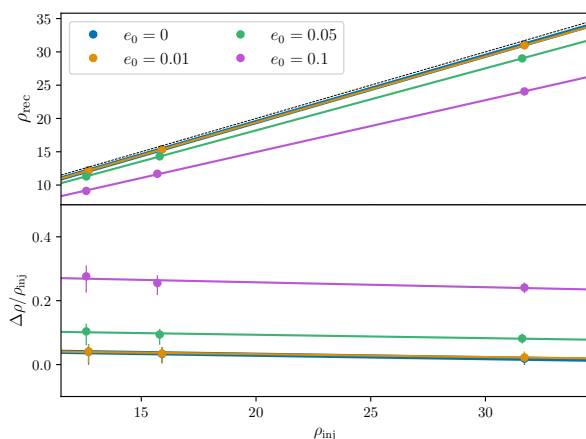


FIG. 12. Median values of recovered SNR (top panel) and SNR loss (bottom panel) as function of the injected SNR for spin-precessing PEs. Different colors refer to different eccentricities as reported in the legend.

ter. However, we also find that the parameters of eccentric binaries with $e_0 \lesssim 0.01$ are robustly determined by a quasi-circular and spinning waveform at $\text{SNR} \lesssim 32$. Under these conditions, eccentric non-spinning BNS signals appear well reproduced by non-precessing quasi-circular templates, but higher SNRs are expected to introduce again significant biases.

Our case study focuses on an unequal-mass BNS with intrinsic parameters compatible with GW170817, including the considered eccentricities [11]. We performed full Bayesian PEs of mock signals at SNR 12.7, 15.9, 31.7 us-

ing the state-of-art EOB model **TEOBResumS-Dalí** with either eccentricity or spin precessional effects. We find that quasi-circular waveform determines fractional SNR losses from a few to $\sim 25\%$ for eccentricities from $e = 0.01$ to 0.1. The SNR losses have an approximate linear dependence with eccentricity in our data, see Eq. (16). The chirp mass is significantly biased towards larger values as the eccentricity increases. This bias can be understood in terms of the eccentric chirp mass parameter \mathcal{M}_{ecc} introduced in [23] (our Eq. (17)). Indeed, for $e_0 \lesssim 0.05$ we recover values of \mathcal{M} that are consistent with \mathcal{M}_{ecc} within their 90% CI. The eccentric chirp mass argument however does not provide a quantitative prediction for the bias for larger eccentricities $e_0 \gtrsim 0.1$. On the one hand, these eccentricities are out of the regime of validity of Eq. (17); on the other hand there is a strong degeneracy with the mass ratio. The mass ratio is degenerate with the eccentric chirp mass and can reach unphysically large values for BNS to reproduce the eccentricity effect. This effect can hamper real-signal analyses and lead to an incorrect interpretation of the source. Large mass ratios would favour a BH interpretation for the primary compact object and a unknown companion, even if the reduced tidal parameter can be measured. We cannot confirm the simple quadratic scaling with eccentricity of Cho [24] for the chirp mass bias because our bias is strongly degenerated with the mass ratio. The effective spin parameter is always inferred as positive and up $\chi_{\text{eff}} \sim 0.8$ for $e_0 \lesssim 0.1$. This suggests that repulsive spin-orbits interactions are effectively counteracting the attractive effect of the larger chirp mass and reduced tidal parameter for the fitting of the eccentric data. The inclusion of spin precession in the waveform is also insufficient to capture eccentricity effects. Therefore, we conclude that the spin precession cannot mimic eccentricity for long signals as in our analyses, since the effects have two different timescales. Furthermore, this case study suggests that the eccentricity of GW170817 is $e_0 < 0.05$, confirming [11], otherwise unphysically large values of the mass ratio may have been observed. In the PE of GW170817 two different priors for the spins have been considered [8], while in all our analyses we adopt the high-spin priors. We are expecting that employing low-spin priors may lead to larger biases in the inferred mass ratio, due to its degeneracy with the effective spin parameter, which may act to compensate for unmodeled eccentric effects.

We conclude that high-precision observations with both upcoming advanced [67–69] and next generation [70–75] detectors are likely to require standardized and accurate eccentric BNS waveforms. While the latter are available in **TEOBResumS-Dalí** the computational cost of waveform generation and inference should be improved in the near future. In the eccentric case, **TEOBResumS-Dalí** cannot yet take advantage of acceleration methods like the post-adiabatic [52] and EOB-SPA [53], although this effect can be incorporated in reduced-order/machine learning models [76]. On the inference side, speed up techniques such as relative binning [77, 78]

can not be employed yet, because a frequency domain description of the model is needed. We could instead consider to use Reduced Order Quadrature [79–81] or RIFT [82–85].

Future work will be focused on a more systematic exploration of different BNS configurations and waveform effects. An important aspect neglected here is the inclusion of higher modes which may enhance the performance of the spin-precessing waveform in capturing the eccentric feature of the signal. Higher modes are available in `TEOBResumS-DaLi` but increase the cost of the inference. Similarly, work is ongoing in exploring inference with eccentric and spinning waveform. Again, there is no conceptual difficulty in performing these analyses with `TEOBResumS-DaLi` but their increased computational cost.

ACKNOWLEDGMENTS

The authors thank Gregorio Carullo, Axel Kuch, Jake Lange and Nicolo’ Venuti for early contributions and discussions on this project. GH and SB acknowledge support by the EU Horizon under ERC Consolidator Grant, no. InspiReM-101043372. SB and MB acknowledge support by the EU H2020 under ERC Starting Grant, no. BinGraSp-714626. MB and RG acknowledge support by the Deutsche Forschungsgemeinschaft (DFG) under Grant No. 406116891 within the Research Training Group RTG 2522/1. RG acknowledges support from NSF Grant PHY-2020275 (Network for Neutrinos, Nuclear Astrophysics, and Symmetries (N3AS)).

This research has made use of data obtained from the Gravitational Wave Open Science Center [86], a service of LIGO Laboratory, the LIGO Scientific Collaboration, the Virgo Collaboration, and KAGRA. This material is based upon work supported by NSF’s LIGO Laboratory, which is a major facility fully funded by the National Science Foundation. LIGO Laboratory and Advanced LIGO are funded by the United States

National Science Foundation (NSF) as well as the Science and Technology Facilities Council (STFC) of the United Kingdom, the Max-Planck-Society (MPS), and the State of Niedersachsen/Germany for support of the construction of Advanced LIGO and construction and operation of the GEO600 detector. Additional support or Advanced LIGO was provided by the Australian Research Council. Virgo is funded through the European Gravitational Observatory (EGO), by the French Centre National de Recherche Scientifique (CNRS), the Italian Istituto Nazionale di Fisica Nucleare (INFN) and the Dutch Nikhef, with contributions by institutions from Belgium, Germany, Greece, Hungary, Ireland, Japan, Monaco, Poland, Portugal, Spain. KAGRA is supported by Ministry of Education, Culture, Sports, Science and Technology (MEXT), Japan Society for the Promotion of Science (JSPS) in Japan; National Research Foundation (NRF) and Ministry of Science and ICT (MSIT) in Korea; Academia Sinica (AS) and National Science and Technology Council (NSTC) in Taiwan.

Simulations were performed on SuperMUC-NG at the Leibniz-Rechenzentrum (LRZ) Munich and on the national HPE Apollo Hawk at the High Performance Computing Center Stuttgart (HLRS). The authors acknowledge the Gauss Centre for Supercomputing e.V. (www.gauss-centre.eu) for funding this project by providing computing time on the GCS Supercomputer SuperMUC-NG at LRZ (allocations `pn36go`, `pn36jo` and `pn68wi`). The authors acknowledge HLRS for funding this project by providing access to the supercomputer HPE Apollo Hawk under the grant number IN-TRHYG UE/44215 and MAGNETIST/44288. Computations were also performed on the ARA cluster at Friedrich Schiller University Jena and on the Tullio INFN cluster at INFN Turin. The ARA cluster is funded in part by DFG grants INST 275/334-1 FUGG and INST 275/363-1 FUGG, and ERC Starting Grant, grant agreement no. BinGraSp-714626.

`TEOBResumS` is publicly available at

<https://bitbucket.org/teobresums>

`bajes` is publicly available at:

<https://github.com/matteobreschi/bajes>

-
- [1] X. Zhu, E. Thrane, S. Osłowski, Y. Levin, and P. D. Lasky, *Phys. Rev. D* **98**, 043002 (2018), arXiv:1711.09226 [astro-ph.HE].
 - [2] J. J. Andrews and I. Mandel, *Astrophys. J. Lett.* **880**, L8 (2019), arXiv:1904.12745 [astro-ph.HE].
 - [3] E. A. Huerta and D. A. Brown, *Phys. Rev. D* **87**, 127501 (2013), arXiv:1301.1895 [gr-qc].
 - [4] A. H. Nitz, A. Lenon, and D. A. Brown, *Astrophys. J.* **890**, 1 (2019), arXiv:1912.05464 [astro-ph.HE].
 - [5] R. Dhurkunde and A. H. Nitz, (2023), arXiv:2311.00242 [astro-ph.HE].
 - [6] B. P. Abbott et al. (LIGO Scientific, Virgo), *Astrophys. J.* **883**, 149 (2019), arXiv:1907.09384 [astro-ph.HE].
 - [7] I. M. Romero-Shaw, P. D. Lasky, and E. Thrane, *Mon. Not. Roy. Astron. Soc.* **490**, 5210 (2019), arXiv:1909.05466 [astro-ph.HE].
 - [8] B. P. Abbott et al. (LIGO Scientific, Virgo), *Phys. Rev. Lett.* **119**, 161101 (2017), arXiv:1710.05832 [gr-qc].
 - [9] B. P. Abbott et al. (LIGO Scientific, Virgo), *Astrophys. J. Lett.* **851**, L16 (2017), arXiv:1710.09320 [astro-ph.HE].
 - [10] B. P. Abbott et al. (LIGO Scientific, Virgo), *Astrophys. J. Lett.* **892**, L3 (2020), arXiv:2001.01761 [astro-ph.HE].
 - [11] A. K. Lenon, A. H. Nitz, and D. A. Brown, *Mon. Not. Roy. Astron. Soc.* **497**, 1966 (2020), arXiv:2005.14146 [astro-ph.HE].
 - [12] I. M. Romero-Shaw, N. Farrow, S. Stevenson, E. Thrane, and X.-J. Zhu, *Mon. Not. Roy. Astron. Soc.* **496**, L64 (2020), arXiv:2001.06492 [astro-ph.HE].

- [13] V. Gayathri, J. Healy, J. Lange, B. O'Brien, M. Szczepanczyk, I. Bartos, M. Campanelli, S. Klimentko, C. O. Lousto, and R. O'Shaughnessy, *Nature Astron.* **6**, 344 (2022), arXiv:2009.05461 [astro-ph.HE].
- [14] V. Gayathri, J. Healy, J. Lange, B. O'Brien, M. Szczepanczyk, I. Bartos, M. Campanelli, S. Klimentko, C. O. Lousto, and R. O'Shaughnessy, *Astrophys. J. Lett.* **908**, L34 (2021), arXiv:2009.14247 [astro-ph.HE].
- [15] I. M. Romero-Shaw, P. D. Lasky, and E. Thrane, *Astrophys. J. Lett.* **921**, L31 (2021), arXiv:2108.01284 [astro-ph.HE].
- [16] E. O'Shea and P. Kumar, *Phys. Rev. D* **108**, 104018 (2023), arXiv:2107.07981 [astro-ph.HE].
- [17] R. Gamba, M. Breschi, G. Carullo, S. Albanesi, P. Rettegno, S. Bernuzzi, and A. Nagar, *Nature Astron.* **7**, 11 (2023), arXiv:2106.05575 [gr-qc].
- [18] I. M. Romero-Shaw, P. D. Lasky, and E. Thrane, *Astrophys. J.* **940**, 171 (2022), arXiv:2206.14695 [astro-ph.HE].
- [19] H. L. Iglesias et al., *Astrophys. J.* **972**, 65 (2024), arXiv:2208.01766 [gr-qc].
- [20] A. Bonino, R. Gamba, P. Schmidt, A. Nagar, G. Pratten, M. Breschi, P. Rettegno, and S. Bernuzzi, *Phys. Rev. D* **107**, 064024 (2023), arXiv:2207.10474 [gr-qc].
- [21] J. Calderón Bustillo, N. Sanchis-Gual, A. Torres-Forné, and J. A. Font, *Phys. Rev. Lett.* **126**, 201101 (2021), arXiv:2009.01066 [gr-qc].
- [22] I. M. Romero-Shaw, P. D. Lasky, E. Thrane, and J. C. Bustillo, *Astrophys. J. Lett.* **903**, L5 (2020), arXiv:2009.04771 [astro-ph.HE].
- [23] M. Favata, C. Kim, K. G. Arun, J. Kim, and H. W. Lee, *Phys. Rev. D* **105**, 023003 (2022), arXiv:2108.05861 [gr-qc].
- [24] H.-S. Cho, *Phys. Rev. D* **105**, 124022 (2022), arXiv:2205.12531 [gr-qc].
- [25] E. A. Huerta et al., *Phys. Rev. D* **97**, 024031 (2018), arXiv:1711.06276 [gr-qc].
- [26] Z. Cao and W.-B. Han, *Phys. Rev. D* **96**, 044028 (2017), arXiv:1708.00166 [gr-qc].
- [27] D. Chiamello and A. Nagar, *Phys. Rev. D* **101**, 101501 (2020), arXiv:2001.11736 [gr-qc].
- [28] A. Nagar and P. Rettegno, *Phys. Rev. D* **104**, 104004 (2021), arXiv:2108.02043 [gr-qc].
- [29] Q. Yun, W.-B. Han, X. Zhong, and C. A. Benavides-Gallego, *Phys. Rev. D* **103**, 124053 (2021), arXiv:2104.03789 [gr-qc].
- [30] A. Ramos-Buades, A. Buonanno, M. Khalil, and S. Ossokine, *Phys. Rev. D* **105**, 044035 (2022), arXiv:2112.06952 [gr-qc].
- [31] A. Nagar, R. Gamba, P. Rettegno, V. Fantini, and S. Bernuzzi, *Phys. Rev. D* **110**, 084001 (2024), arXiv:2404.05288 [gr-qc].
- [32] X. Liu, Z. Cao, and Z.-H. Zhu, *Class. Quant. Grav.* **41**, 195019 (2024), arXiv:2310.04552 [gr-qc].
- [33] A. Gamboa et al., (2024), arXiv:2412.12823 [gr-qc].
- [34] M. d. L. Planas, A. Ramos-Buades, C. García-Quirós, H. Estellés, S. Husa, and M. Haney, (2025), arXiv:2503.13062 [gr-qc].
- [35] A. Ramos-Buades, A. Buonanno, and J. Gair, *Phys. Rev. D* **108**, 124063 (2023), arXiv:2309.15528 [gr-qc].
- [36] A. G. Abac et al. (LIGO Scientific, KAGRA, VIRGO), *Astrophys. J.* **973**, 132 (2024), arXiv:2308.03822 [astro-ph.HE].
- [37] B. Gadre, K. Soni, S. Tiwari, A. Ramos-Buades, M. Haney, and S. Mitra, *Phys. Rev. D* **110**, 044013 (2024), arXiv:2405.04186 [gr-qc].
- [38] S. Bhaumik et al., (2024), arXiv:2410.15192 [gr-qc].
- [39] R. Gamba, D. Chiamello, and S. Neogi, *Phys. Rev. D* **110**, 024031 (2024), arXiv:2404.15408 [gr-qc].
- [40] S. Albanesi, R. Gamba, S. Bernuzzi, J. Fontbuté, A. Gonzalez, and A. Nagar, (2025), arXiv:2503.14580 [gr-qc].
- [41] M. Favata, *Phys. Rev. Lett.* **112**, 101101 (2014), arXiv:1310.8288 [gr-qc].
- [42] R. Gamba and S. Bernuzzi, *Phys. Rev. D* **107**, 044014 (2023), arXiv:2207.13106 [gr-qc].
- [43] A. Nagar et al., *Phys. Rev. D* **98**, 104052 (2018), arXiv:1806.01772 [gr-qc].
- [44] T. Damour and A. Nagar, *Phys. Rev. D* **90**, 044018 (2014), arXiv:1406.6913 [gr-qc].
- [45] A. Nagar, D. Chiamello, R. Gamba, S. Albanesi, S. Bernuzzi, V. Fantini, M. Panzeri, and P. Rettegno, *Phys. Rev. D* **111**, 064050 (2025), arXiv:2407.04762 [gr-qc].
- [46] A. Nagar, P. Rettegno, R. Gamba, S. Albanesi, A. Albertini, and S. Bernuzzi, *Phys. Rev. D* **108**, 124018 (2023), arXiv:2304.09662 [gr-qc].
- [47] G. Riemenschneider, P. Rettegno, M. Breschi, A. Albertini, R. Gamba, S. Bernuzzi, and A. Nagar, *Phys. Rev. D* **104**, 104045 (2021), arXiv:2104.07533 [gr-qc].
- [48] A. Nagar, G. Pratten, G. Riemenschneider, and R. Gamba, *Phys. Rev. D* **101**, 024041 (2020), arXiv:1904.09550 [gr-qc].
- [49] S. Bernuzzi, A. Nagar, T. Dietrich, and T. Damour, *Phys. Rev. Lett.* **114**, 161103 (2015), arXiv:1412.4553 [gr-qc].
- [50] S. Akçay, S. Bernuzzi, F. Messina, A. Nagar, N. Ortiz, and P. Rettegno, *Phys. Rev. D* **99**, 044051 (2019), arXiv:1812.02744 [gr-qc].
- [51] R. Gamba, S. Akçay, S. Bernuzzi, and J. Williams, *Phys. Rev. D* **106**, 024020 (2022), arXiv:2111.03675 [gr-qc].
- [52] A. Nagar and P. Rettegno, *Phys. Rev. D* **99**, 021501 (2019), arXiv:1805.03891 [gr-qc].
- [53] R. Gamba, S. Bernuzzi, and A. Nagar, *Phys. Rev. D* **104**, 084058 (2021), arXiv:2012.00027 [gr-qc].
- [54] M. Breschi, R. Gamba, and S. Bernuzzi, *Phys. Rev. D* **104**, 042001 (2021), arXiv:2102.00017 [gr-qc].
- [55] J. Veitch and A. Vecchio, *Phys. Rev. D* **81**, 062003 (2010), arXiv:0911.3820 [astro-ph.CO].
- [56] B. P. Abbott et al. (LIGO Scientific, Virgo), *Class. Quant. Grav.* **37**, 055002 (2020), arXiv:1908.11170 [gr-qc].
- [57] J. Veitch et al., *Phys. Rev. D* **91**, 042003 (2015), arXiv:1409.7215 [gr-qc].
- [58] W. J. Handley, M. P. Hobson, and A. N. Lasenby, *Mon. Not. Roy. Astron. Soc.* **450**, L61 (2015), arXiv:1502.01856 [astro-ph.CO].
- [59] R. Allison and J. Dunkley, *Mon. Not. Roy. Astron. Soc.* **437**, 3918 (2014), arXiv:1308.2675 [astro-ph.IM].
- [60] B. P. Abbott et al. (KAGRA, LIGO Scientific, Virgo), *Living Rev. Rel.* **19**, 1 (2016), arXiv:1304.0670 [gr-qc].
- [61] F. Acernese et al. (VIRGO), *Class. Quant. Grav.* **32**, 024001 (2015), arXiv:1408.3978 [gr-qc].
- [62] B. P. Abbott et al. (LIGO Scientific, Virgo), *Phys. Rev. Lett.* **116**, 061102 (2016), arXiv:1602.03837 [gr-qc].
- [63] B. P. Abbott et al. (LIGO Scientific, Virgo), *Phys. Rev. X* **9**, 031040 (2019), arXiv:1811.12907 [astro-ph.HE].
- [64] R. Abbott et al. (LIGO Scientific, Virgo), *SoftwareX* **13**, 100658 (2021), arXiv:1912.11716 [gr-qc].

- [65] J. S. Speagle, Mon. Not. Roy. Astron. Soc. **493**, 3132 (2020), arXiv:1904.02180 [astro-ph.IM].
- [66] R. Gamba, M. Breschi, S. Bernuzzi, M. Agathos, and A. Nagar, Phys. Rev. D **103**, 124015 (2021), arXiv:2009.08467 [gr-qc].
- [67] J. Aasi et al. (LIGO Scientific), Class. Quant. Grav. **32**, 074001 (2015), arXiv:1411.4547 [gr-qc].
- [68] F. Acernese et al. (VIRGO), Class. Quant. Grav. **32**, 024001 (2015), arXiv:1408.3978 [gr-qc].
- [69] B. P. Abbott et al. (KAGRA, LIGO Scientific, Virgo), Living Rev. Rel. **19**, 1 (2016), arXiv:1304.0670 [gr-qc].
- [70] S. Hild et al., Class. Quant. Grav. **28**, 094013 (2011), arXiv:1012.0908 [gr-qc].
- [71] S. Hild, Class. Quant. Grav. **29**, 124006 (2012), arXiv:1111.6277 [gr-qc].
- [72] M. Punturo et al., Class. Quant. Grav. **27**, 194002 (2010).
- [73] M. Branchesi et al., JCAP **07**, 068 (2023), arXiv:2303.15923 [gr-qc].
- [74] A. Abac et al., (2025), arXiv:2503.12263 [gr-qc].
- [75] D. Reitze et al., Bull. Am. Astron. Soc. **51**, 035 (2019), arXiv:1907.04833 [astro-ph.IM].
- [76] J. Tissino, G. Carullo, M. Breschi, R. Gamba, S. Schmidt, and S. Bernuzzi, Phys. Rev. D **107**, 084037 (2023), arXiv:2210.15684 [gr-qc].
- [77] L. Dai, T. Venumadhav, and B. Zackay, (2018), arXiv:1806.08793 [gr-qc].
- [78] B. Zackay, L. Dai, and T. Venumadhav, (2018), arXiv:1806.08792 [astro-ph.IM].
- [79] P. Canizares, S. E. Field, J. Gair, V. Raymond, R. Smith, and M. Tiglio, Phys. Rev. Lett. **114**, 071104 (2015), arXiv:1404.6284 [gr-qc].
- [80] R. Smith, S. E. Field, K. Blackburn, C.-J. Haster, M. Pürrer, V. Raymond, and P. Schmidt, Phys. Rev. D **94**, 044031 (2016), arXiv:1604.08253 [gr-qc].
- [81] S. Morisaki and V. Raymond, Phys. Rev. D **102**, 104020 (2020), arXiv:2007.09108 [gr-qc].
- [82] C. Pankow, P. Brady, E. Ochsner, and R. O’Shaughnessy, Phys. Rev. D **92**, 023002 (2015), arXiv:1502.04370 [gr-qc].
- [83] J. Lange, R. O’Shaughnessy, and M. Rizzo, (2018), arXiv:1805.10457 [gr-qc].
- [84] D. Wysocki, R. O’Shaughnessy, J. Lange, and Y.-L. L. Fang, Phys. Rev. D **99**, 084026 (2019), arXiv:1902.04934 [astro-ph.IM].
- [85] J. Wofford et al., (2022), arXiv:2210.07912 [gr-qc].
- [86] LIGO Scientific and Virgo Collaboration, <https://www.gw-openscience.org>, Gravitational-Wave Open Science Center.